



HAL
open science

Retrieving mean volumetric properties of multiphase flows from 2D images: A new approach combining deep learning algorithms and 3D modelling

Kassem Dia, Fabrice Lamadie, Johan Debayle

► To cite this version:

Kassem Dia, Fabrice Lamadie, Johan Debayle. Retrieving mean volumetric properties of multiphase flows from 2D images: A new approach combining deep learning algorithms and 3D modelling. Chemical Engineering Science, 2023, 279, pp.118933. 10.1016/j.ces.2023.118933 . emse-04245777

HAL Id: emse-04245777

<https://hal-emse.ccsd.cnrs.fr/emse-04245777>

Submitted on 18 Oct 2023

HAL is a multi-disciplinary open access archive for the deposit and dissemination of scientific research documents, whether they are published or not. The documents may come from teaching and research institutions in France or abroad, or from public or private research centers.

L'archive ouverte pluridisciplinaire **HAL**, est destinée au dépôt et à la diffusion de documents scientifiques de niveau recherche, publiés ou non, émanant des établissements d'enseignement et de recherche français ou étrangers, des laboratoires publics ou privés.

1 **Retrieving mean volumetric properties of multiphase flows from 2D images: a new approach combining deep learning**
2 **algorithms and 3D modelling**

3 Kassem Dia^{1,2}, Fabrice Lamadie¹ and Johan Debayle²

4 1 CEA, DES, ISEC, DMRC, Univ Montpellier, Marcoule, France.

5 2 MINES Saint-Etienne, SPIN/LGF UMR CNRS 5307, 158 cours Fauriel, Saint-Etienne, France.

6 Contributing authors: kassem.dia@cea.fr; fabrice.lamadie@cea.fr; debayle@emse.fr;

7 **Abstract**

8 Measuring the morphological properties of complex multiphase systems is a crucial problem in many areas of
9 science and industry and is particularly difficult in dense environments with limited optical access. This paper
10 presents a new approach capable of extracting three-dimensional (3D) information from spherical particle
11 systems based solely on two-dimensional (2D) projections of the system. Synthetic images of the system are
12 generated using a stochastic geometrical model from a simulated 3D particle system with the same geometrical
13 features as the studied system, which is projected into 2D images labeled with the appropriate 3D information.
14 These images are then fed to a convolutional neural network (CNN) for training before being tested on synthetic
15 and experimental images. Validation results show that this technique successfully predicts the mean features of
16 the studied systems, even for dense environments with overlapping particles, with high computational efficiency.

17

18 **Keywords:** Convolutional neural network, Particle systems, Stochastic Geometry, 3D Modelling.

19

20 **1. Introduction**

21 Complex particulate systems are an important and widely studied feature of many industrial processes (Black et
22 al., 1996; Gianinoni et al., 2003; Honkanen et al., 2010) and research projects (Clift, R., Grace, J. R., & Weber,
23 2005; Poelma, 2020). These systems are generally defined as mixtures of two or more substances where one is
24 suspended in another, either a gas in a liquid (bubble flow) (Juliá et al., 2005; Karn et al., 2015; Lau et al., 2013),
25 a solid in a liquid (Kavanaugh et al., 1980; Yu et al., 2009), or one immiscible liquid in another (emulsions) (Huang
26 et al., 2001; Maaß et al., 2011).

27 Measuring the properties of these systems is essential to optimize and improve the performance of many processes
28 involving multiphase flows (Emmerich et al., 2019; Panckow et al., 2017). In chemical engineering for example,
29 knowledge of particle spatial distributions is crucial to calculate mass and heat transfer rates and the reaction
30 kinetics governing the efficiency of the process. In this context, the most important properties are the particle size
31 distribution (PSD) of the dispersed field, the mean characteristic diameters (d_{43} , d_{32} , d_{10} , ...), the volume fraction
32 of the dispersed phase (ϕ), and morphological information such as the shape and irregularity of the particles.

33 Extracting this information is a non-trivial problem and many approaches have been investigated in the literature.
34 Laser-based methods involve the analysis of scattered light from a laser beam passing through the system. One of
35 the most popular in-line method is focused beam reflectance measurement (FBRM) (Heath et al., 2002; Ruf et al.,
36 2000), in which a highly focused rotating laser beam is passed at a fixed speed over the suspended particles and
37 the duration of the backscattered light is measured. Although this only provides information on the chord length
38 distribution of the particles, and post processing is required to retrieve the PSD, this technique has successfully
39 been used to measure droplet size distributions in water oil emulsions (Boxall et al., 2010) and micro-bubble size
40 distributions in air flotation processes (Couto et al., 2009), and has proven particularly valuable for the
41 characterization of crystal-like particles (Acevedo et al., 2021; Heinrich and Ulrich, 2012; Pandalaneni and
42 Amamcharla, 2016; Pandit et al., 2019). The second widely used laser-based technique in this context is digital in-
43 line holography (DIH), otherwise known as lens-free imaging (Darakis et al., 2010; Lamadie et al., 2012), in which
44 particle characteristics are estimated from the laser diffraction patterns of the system. This approach has been used
45 to study the position and size of particles in pipe flows (Sentis et al., 2017), microscopic setups (Sheng et al.,
46 2006), and sprays (Yang and Kang, 2011), combined with a machine learning algorithm to study non-uniformly
47 shaped particles (Shao et al., 2020). However, while DIH is very efficient for 3D positioning and PSD
48 measurements, it can only be used in optical dilute media.

49 Imaging-based methods generally provide richer information than other available techniques and therefore more
50 widely used. Image analysis algorithms combined with direct imaging can be used to measure properties other
51 than the PSD (Maaß et al., 2011), such as the volume fraction of the dispersed phase (Karn et al., 2015),
52 morphological information on irregular particles (Suh et al., 2021), and the presence of clusters (Zhang et al.,
53 2012). The image processing algorithms used have included deterministic methods such as the Hough transform
54 (Yu et al., 2009), watershed segmentation (Chen et al., 2004), more sophisticated approaches to deal with
55 overlapping particles (de Langlard et al., 2018a; Zafari et al., 2020; Zhang et al., 2012; Zou et al., 2021), and
56 recently, machine learning methods (Cui et al., 2022; Haas et al., 2020; Kim and Park, 2021; Li et al., 2021). Most

57 of these techniques extract 2D information from the detection of individual particles and cannot measure 3D
58 properties. Although 3D information can be retrieved from multiple viewpoints, this requires a complex imaging
59 setup with multiple optical access points (Wang et al., 2022; Xue et al., 2014), which is not always desirable or
60 possible.

61 This article presents a new approach in which a deep learning algorithm is combined with stochastic geometrical
62 models to extract 3D properties from 2D projected images of the system. The 3D stochastic geometrical model is
63 used to generate a huge set of synthetic 2D images labeled with the 3D geometrical properties of the particle field
64 and with the same geometrical properties as experimental images. This model can be used to reproduce any 3D
65 particle field and generate 2D projections suitable to train a convolutional neural network (CNN) (Dia et al., 2022).
66 To the best of our knowledge, this type of approach has only previously been used by Fend et al. (Fend et al.,
67 2021) to reconstruct highly porous 3D structures from focused ion beam scanning electron microscopy data.

68 The paper is divided into six sections. The following methods section provides a brief reminder of the principles
69 of stochastic geometrical modelling and a description of the chosen machine learning algorithm. The third
70 section describes the parameters chosen to measure the performance of the network and the results of tests on
71 representative simulated flows. The fourth section presents experimental results for 3D dispersed phase volume
72 fractions and PSDs retrieved from highly concentrated particle systems. The results obtained for experimental
73 and liquid-liquid system images are presented in section 5 and the final section is an overall conclusion with
74 perspectives.

75 **Computational methods**

76 As mentioned above, the proposed approach (Figure 1) involves two computational tools, a stochastic geometrical
77 model and a CNN.

78 For the synthetic images to be representative, the simulated particle system should have the same geometrical
79 properties as the studied system, i.e. be statistically representative of the observed particle field. The 3D stochastic
80 model used to generate the images should consist of a hard-core model of the particles, in this case spherical, that
81 accounts for the statistical properties of the dispersed phase by eliminating all particle-particle and particle-wall
82 interactions. Matérn type II point processes (Matérn, 2014) were therefore chosen to generate the synthetic images.

83 Matérn type II point processes are derived from an underlying homogeneous Poisson point process in \mathbb{R}^d with
84 intensity λ . A point process is simulated and a thinning rule is applied based on a hard-core distance ($r > 0$)

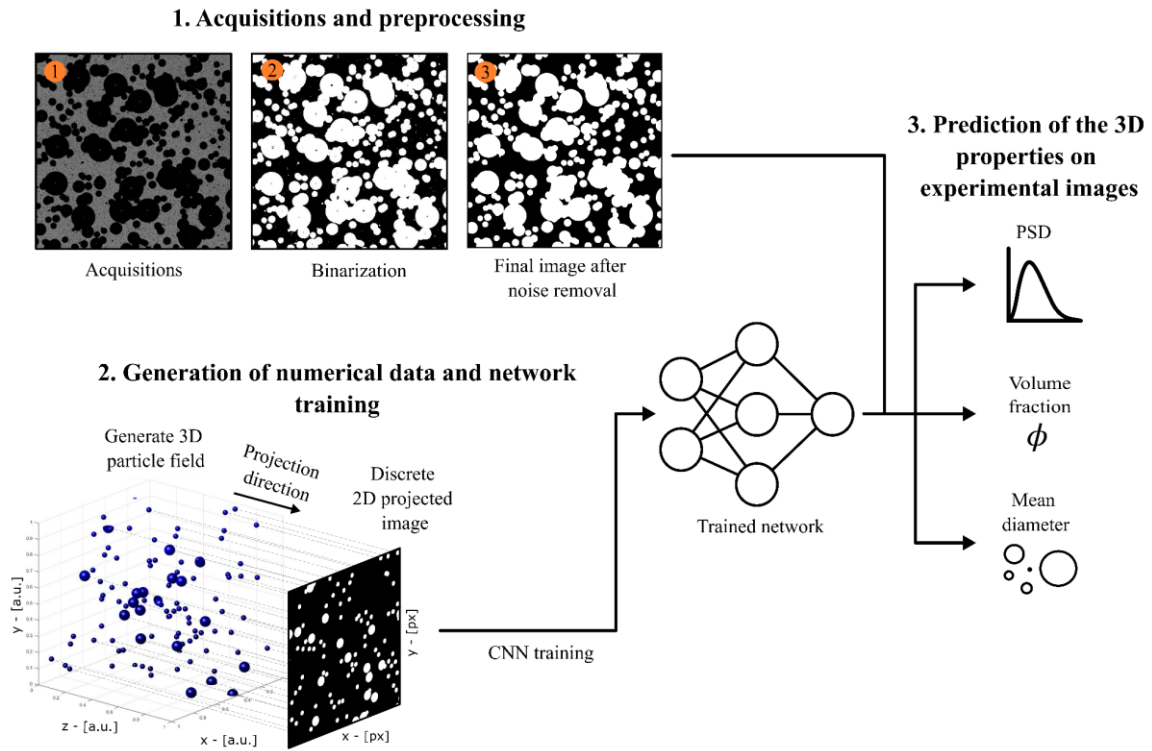
85 between the generated points, which removes the last arriving point from any pair of points less than $2r$ apart.
 86 This process can be considered a marked point process where the first mark r (constant and positive) represents
 87 the hard-core radius and the second mark is the time of arrival of the points modeled using a uniform random
 88 variable.

89 The generation process for the synthetic images thus involves the following steps:

- 90 1. Choosing a 3D domain $W = \mathbb{R}^2 \times [0, l]$, where $l > 0$ is the length of the projection direction, consistent
 91 with the dimensions of the actual measurement volume.
- 92 2. Randomly positioning the particles inside W according to a Poisson point process with intensity λ . Each
 93 point is marked with a radius r_i , and a time of birth $t_i, \forall i \in \{1, \dots, n_p\}$.
- 94 3. Applying two thinning rules: *i*) Matérn's thinning rule, *i.e.* eliminating the last arriving point
 95 ($\max(t_1, t_2)$) of pairs (x_1, r_1, t_1) (x_2, r_2, t_2) with $\|x_1 - x_2\|_2 \leq r_1 + r_2$, and *ii*) de Langlard et al.'s thinning
 96 rule (de Langlard et al., 2018b) to eliminate particle–boundary interactions by removing points with a
 97 probability $1 - \exp(-U(x, r, t))$, where $U: W \times \mathbb{R}^+ \times [0, 1] \rightarrow \mathbb{R}^+ \cup \{+\infty\}$ is an interaction function.
- 98 4. Projecting the generated 3D particle field orthogonally onto a 2D grid to create a single synthetic image, as
 99 shown in Figure 1.

100 The model generates continuous-valued particles that are later discretized when the synthetic images are generated;
 101 the resolution of the images can thus be adjusted as required. The whole process is repeated N times to assemble
 102 a training database, and the geometrical properties of each 3D model (size distribution, spatial distribution, etc.)
 103 are all stored along with the 2D images (cf. Figure 1, second step). Further details about the stochastic 3D model
 104 used here can be found in de Langlard et al. (de Langlard et al., 2018b).

105 This model can also be used when the distances between points are non-deterministic, and is therefore applicable
 106 to real systems. As demonstrated by Stoyan and Stoyan (Stoyan and Stoyan, 1985), the thinning rules are
 107 generalizable to cases in which the r marks follow a given probability law, and generalized expressions can always
 108 be obtained for distribution parameters such as the retention function and the intensity after thinning. The model
 109 can also be extended by changing the shape of the particles.



110

111 Figure 1. Schematic outline of the main steps of the workflow. 1- Acquisition and preprocessing of experimental images. 2-

112 Generation of a simulated dataset and training of the neural network. 3- Prediction of 3D properties from experimental data.

113 Note that the training images must be of the same type as the experimental ones, and since a stochastic model is
 114 used, only binary images can be used to train the CNN. This means that the experimental data have to be acquired
 115 with a backlight setup based on a telecentric lens (cf. section 4) to limit blurring and perspective effects. The
 116 images also have to be binarized and denoised before being processed by the CNN (see Figure 1).

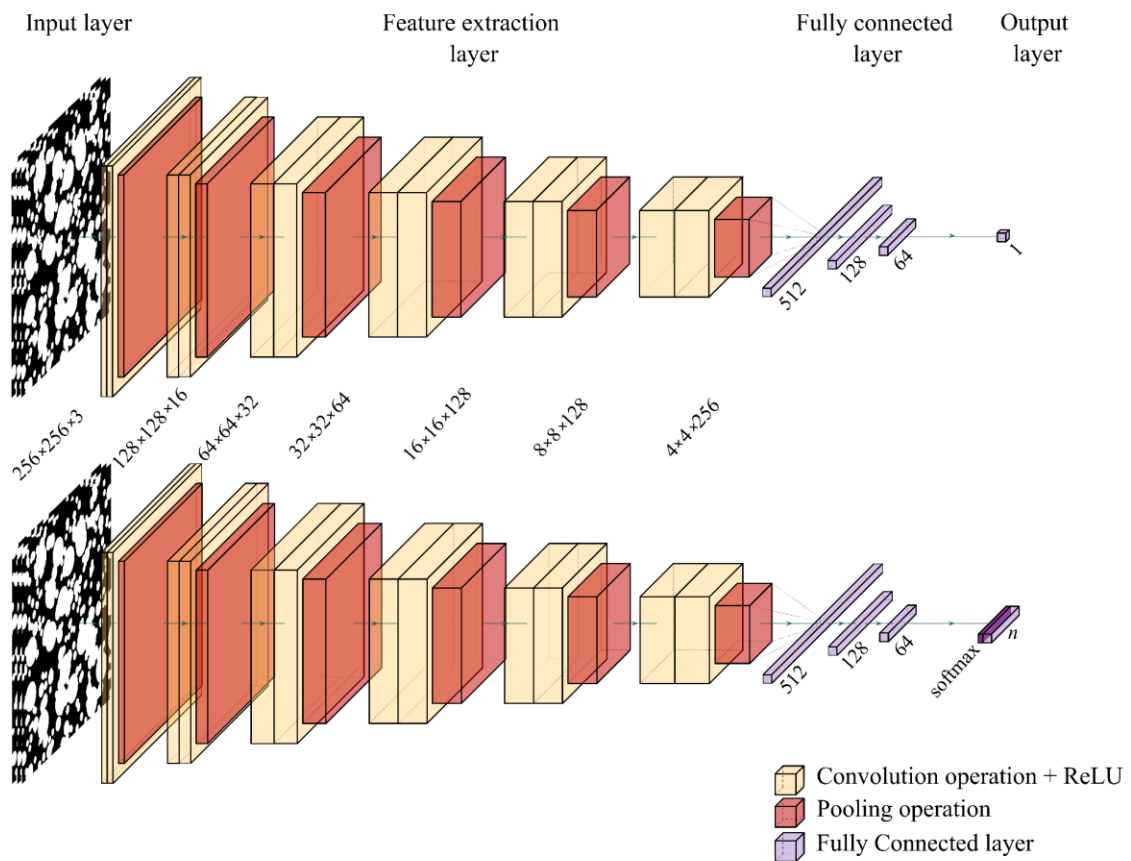
117 The CNN is the second pillar of the proposed approach. Convolutional neural networks are a class of deep learning
 118 algorithms designed to process data with a grid-like topology (*e.g.* images, grid cells, financial series...). These
 119 algorithms are classed as supervised in the sense that they require both data and labels to be trained to perform a
 120 given task. They can be used to solve classification and regression problems but here, only regression CNNs were
 121 considered, because the problem involves continuous values.

122 A CNN broadly consists of four layers (Figure 2):

- 123
- An input layer that processes the data provided to the network.

- 124 • A feature extraction or convolutional layer, which combines convolutional operations, a non-linear
125 activation function (*e.g.* ReLU, sigmoid), and a pooling operator (*e.g.* max pooling, average pooling) to
126 automatically extract relevant features from the images.
- 127 • A fully connected (FC) layer at the end of the network consisting of multiple interconnected neurons
128 whose weights are adjusted to teach the network to identify important features.
- 129 • An output layer, which presents the predictions.

130 Unfortunately, there is no generic way to determine the optimal network shape (*e.g.* the number of convolutional
131 layers, number of neurons, number of layers in the FC layer, the learning rate) in advance. This problem is
132 typically solved using prior experience of CNNs for initial guesses and empirical trials to choose the best
133 architecture. Here, two separate networks were used, one to determine the volume fraction and one to measure
134 the PSD.



135

136 Figure 2. Visualizations of the architectures of the two CNNs used in the study: one to predict the volume fraction (CNN^φ,
137 upper row) used and the other to determine the PSD (CNN^{PSD}, lower row). The plots were generated with PlotNeuralNet

138

(Iqbal, 2018).

- 139 1. The first network, CNN^ϕ (Figure 2, top panel) is used to predict the volume fraction (ϕ) of the dispersed
 140 phase and was trained on volume-fraction labeled images. The input layer consists of three identical $256 \times$
 141 256 images. The feature extraction layer consists of six convolutional layers respectively containing 16,
 142 32, 64, 128, and 256 filters, with a kernel size of 3×3 . These layers also contain an activation function,
 143 ReLU, are followed by a 2×2 max pooling layer, producing flattened feature maps that are fed to the FC
 144 layer. The FC layer contains three sub-layers with 512, 128 and 64 neurons, respectively, and a dropout of
 145 50% is applied after each layer to reduce overfitting. Finally, the output layer consist of a single neuron
 146 representing the predicted value, $\hat{\phi}$.
- 147 2. The second network, CNN^{PSD} (Figure 2, bottom panel), used to predict the 3D PSD, has the same
 148 architecture except for the output layer which is a vector of size n (note that the output size can be adjusted
 149 depending on the studied system). Since the estimated parameter is a distribution, the sum of the elements in
 150 the vector is normalized to 1 using the softmax function.

151 2. Network training strategy

152 After setting the number of layers and the parameters of the CNN, optimal hyper-parameters were determined by
 153 gradient-based optimization. The dataset ($N = 22\,400$) used to train the network was split into three categories;
 154 an initial training set ($N_t = 16\,000$), a validation set ($N_v = 2\,000$) used to monitor the overall performance of
 155 the network at each iteration, and a final testing set ($N_e = 4\,400$) used to evaluate the performance of the
 156 network. All the generated images corresponded to a measurement volume of $25.79 \times 25.79 \times 53 \text{ mm}^3$ in
 157 keeping with the experimental setup. The parameters of the stochastic model were varied uniformly to account
 158 for the variety of possible experimental images in real life applications. The intensity of the particles, λ , was
 159 adjusted between 100 to 250, while the PSD was modeled as a truncated lognormal function, $\mathcal{L}_{tr}(\mu, \sigma^2, a, b)$,
 160 with μ varied randomly from -7.5 to 0.06 , σ from 0 to 2.5 , and a and b equal to 0.005 and 0.08 respectively
 161 (check Table 1).

162 As mentioned above, CNN training datasets have to be labeled with the target information. Here, all the
 163 numerical images were generated over a 5.5 h period and each image, i , was labeled with the corresponding 3D
 164 volume fraction $\phi_i = \frac{v_i}{V_i}$ (with v_i is the volume of the particles, and V_i is total volume) and number weighted
 165 PSD (PSD_i) across n classes.

166

167

Table 1. Details on the synthetic dataset.

	Dataset
#Testing	16000
#Validation	2000
#Testing	4400
ϕ	[0.5 12.2]
Size	$256 \times 256 \times 3$

168

169

The hyper-parameters were then optimized using mean absolute error (MAE) as the loss function. The MAE

170

measures the average absolute difference between true $Y = \{y_1, \dots, y_{N_t}\}$ and predicted values $\hat{Y} = \{\hat{y}_1, \dots, \hat{y}_{N_t}\}$:

171

$$\text{MAE}(Y, \hat{Y}) = \frac{1}{N_t} \sum_i^{N_t} |y_i - \hat{y}_i|,$$

172

Finally, a series of tests were conducted to identify the best number of epochs, the optimal learning rate, and the

173

size of the mini-batches. Slight differences in computational times were observed, so these parameters were

174

optimized as follows:

175

1. Number of epochs: the CNN was trained using mini-batches due to limited computational resources, with

176

one epoch corresponding to one training run over all the mini-batches. The network training convergence

177

was reached after 100 epochs, therefore the number of epochs was then fixed at 150 with a callback to stop

178

the training run if the MAE increased for 10 straight epochs, to avoid overfitting.

179

2. Learning rate: The learning rate was adjusted from a starting value of 10^{-4} , with a decay rate of 20% every

180

50 epochs, down to a final learning rate of 4×10^{-6} ,

181

3. Mini-batch size: the mini-batch size was set to 32.

182

The CNNs were trained using a supercomputer cluster equipped with GPUs each with 640 tensor cores and a

183

memory of 32 GB. The training processes took about 30 min for each CNN.

184

Since the accuracy of the predictions cannot be determined for regression CNNs, the performance of the

185

networks was determined using the MAE and the relative error (RE) for the volume fraction predictions, and

186

using the MAE only for the PSD. Since the volume fraction is a scalar quantity, MAE calculations are

187

straightforward, but for the PSD, which is a vector, the overall MAE, $\overline{\text{MAE}}$, was calculated by comparing the

188

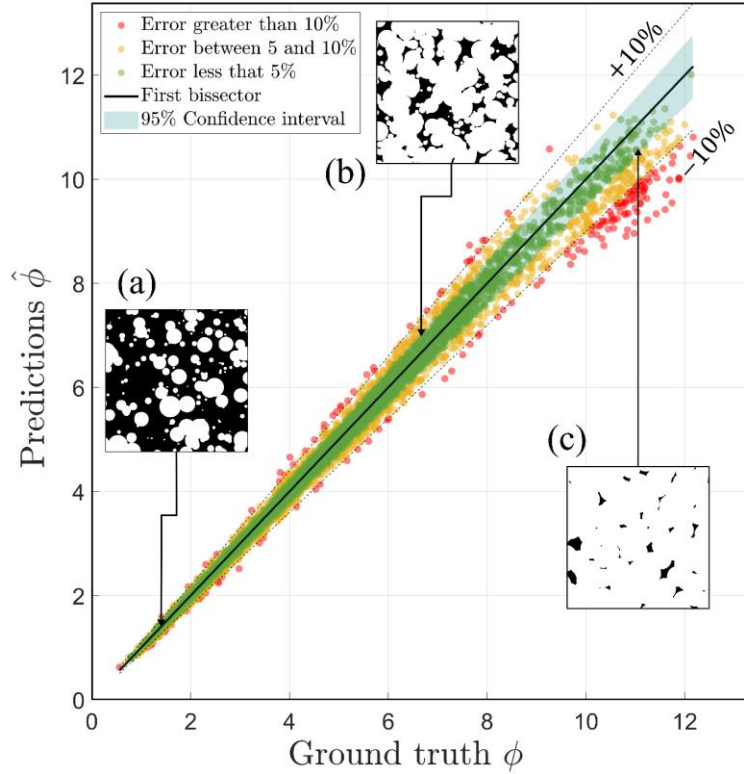
average values of PSD_i and \widehat{PSD}_i .

189

3. Numerical validation

190 The performance of CNN^ϕ was evaluated using the testing dataset, with hold-up values ranging from 0.5 to
 191 12.2%, and the PSD varied between images.

192 The results of the predictions compared to the ground truth are shown in Figure 3. The MAE of 0.21 ± 0.26
 193 highlights the overall accuracy of the network's predictions.



194

195 Figure 3. Scatter plot of the predicted 3D volume fraction $\hat{\phi}$ as a function of the ground truth ϕ . The insets show examples of
 196 the images from the testing dataset, with $\phi_{(a)} = 1.3\%$, $\phi_{(b)} = 5\%$, and $\phi_{(c)} = 11.3\%$, respectively. The points are color
 197 coded according to the relative error of the predictions, $RE_i = \frac{\phi_i - \hat{\phi}_i}{\phi_i}$, green if $|RE_i| \leq 0.05$, orange if $0.05 < |RE_i| \leq 0.1$,
 198 and red if $|RE_i| > 0.1$. The dashed lines border the predictions with less than 10% RE and the first bisector is represented by
 199 a solid line. The shaded green area represents the 95% confidence interval of the predictions.

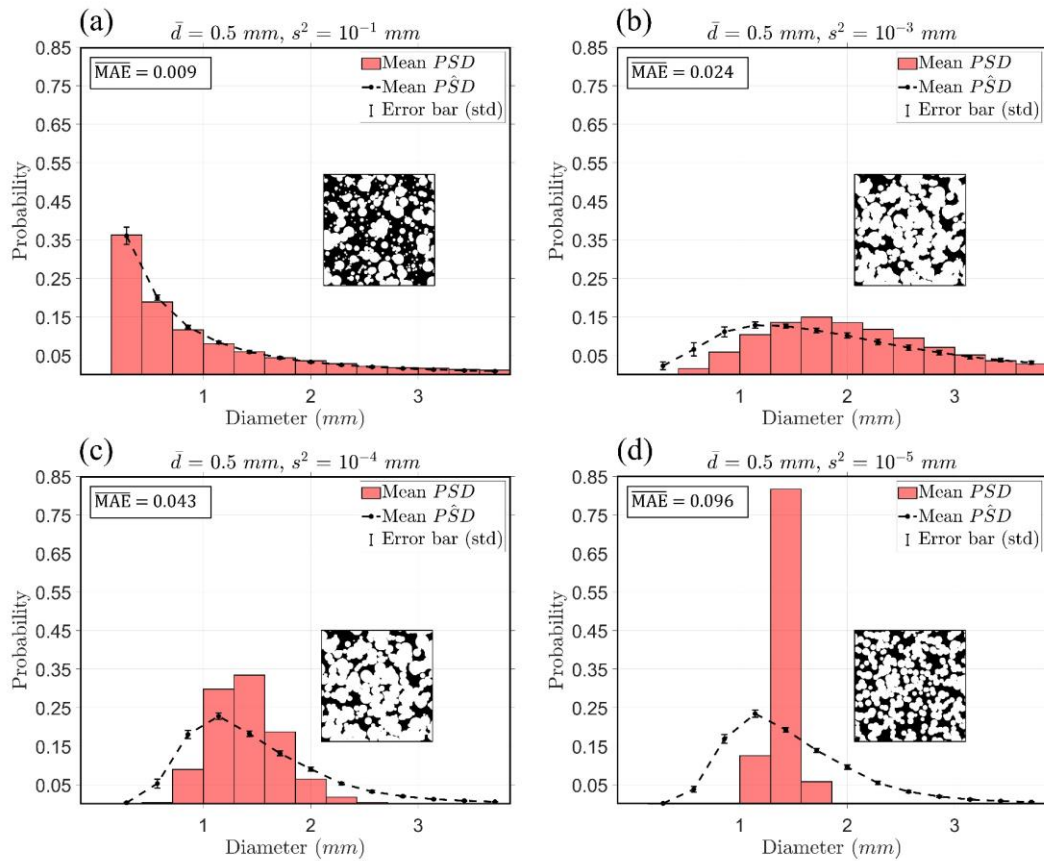
200 The density of particles in the images naturally increases with the particle volume fraction, making the images
 201 more complex to process (compare insets (c) and (a) in Figure 3, for instance). Significant patterns that the
 202 network uses to refine its predictions may also disappear. Nevertheless, while the relative errors of the
 203 predictions increase with the particle volume fraction, they are all of the correct order of magnitude, confirming
 204 the robustness of the approach. Figure 3 shows for instance that below $\phi = 10\%$ (93% occupied area in the
 205 images), more than 77% of the network predictions are within the 95% confidence interval.

206 To validate the PSD estimates, 50 further sets of 100 images were generated using a truncated lognormal
 207 function with a fixed particle intensity of $\lambda = 200$. The variance s^2 and the mean diameter \bar{d} were chosen to
 208 cover a wide range of narrow and wide unimodal distributions with mean diameters ranging from 500 μm to
 209 5 mm. Predictions were made for each image using the trained CNN^{PSD} and binned in 13 size classes. The
 210 predictions were then averaged (\overline{PSD}) and compared to the ground truth distribution (PSD) obtained from the
 211 corresponding function.

212 The \overline{MAE} values obtained (check Table 2) were lower than 0.03 in 60% of the considered cases, corresponding
 213 to good agreement between the predicted and ground truth distributions (see Figure 4). For the broadest
 214 distributions (variance $\geq 10^{-3}$), corresponding to a maximum occupied surface fraction of about 80%, 82% of
 215 the \overline{MAE} values are less than 0.03. As expected on the other hand, the network performs less well for very
 216 narrow distributions (variances range from 10^{-5} to 10^{-4}), as there were no such distributions in the training
 217 dataset. The results for four typical cases are presented in Figure 4.

218 Table 2. Overall MAE for PSD predictions from all 50 simulations. Results for the four cases presented in Figure 4 are
 219 highlighted in bold.

Variance s^2						
	(mm)	10^{-5}	10^{-4}	10^{-3}	10^{-2}	10^{-1}
Mean \bar{d}	(mm)					
0.5		0.059	0.021	0.009	0.009	0.009
1.0		0.085	0.027	0.009	0.009	0.009
1.5		0.071	0.027	0.012	0.010	0.010
2.0		0.096	0.043	0.014	0.011	0.011
2.5		0.114	0.068	0.018	0.011	0.011
3.0		0.115	0.080	0.024	0.013	0.011
3.5		0.123	0.083	0.034	0.014	0.012
4.0		0.115	0.077	0.041	0.015	0.012
4.5		0.114	0.088	0.047	0.018	0.013
5.0		0.131	0.108	0.058	0.022	0.013



221

222 Figure 4. Comparison of CNN^{PSD} predictions with the ground truth for a representative selection of simulated mean particle
 223 diameters and particle size variances. The inset in each panel is a typical image of the corresponding particle field. Error bars
 224 represent the standard deviations of the predictions.

225 4. Experimental validation

226 After validating the approach on simulated data, experimental validations were performed, first using calibrated
 227 spherical poly(methyl methacrylate) (PMMA) beads (diameter precision $\pm 1\%$) submerged in brine stirred in a
 228 rectangular mockup unit and second, using existing data from an emulsion in a cylindrical stirred tank.

229 4.1. Validation with calibrated beads

230 Particle suspensions are particularly convenient for validation as they reproduce the main features of two-phase
 231 flows but without the coalescence and breakage events that frequently occur with bubbles and droplets. With
 232 solid particles moreover, the properties of the dispersed phase are clearly defined. Here, calibrated spherical
 233 PMMA particles were stirred in 1 L of brine (330 g NaCl dissolved in 1 L of water) using a four blade propeller.

234 Brine was chosen so that the density of the continuous phase could be adjusted to that of the dispersed phase to
 235 avoid creaming effects and guarantee a homogeneous dispersion of the particles in the flow.

236 A lognormal distribution of particle sizes cannot be reproduced experimentally using calibrated beads because of
 237 time and cost constraints (a 1.48% volume fraction corresponds to about 10000 particles for instance).

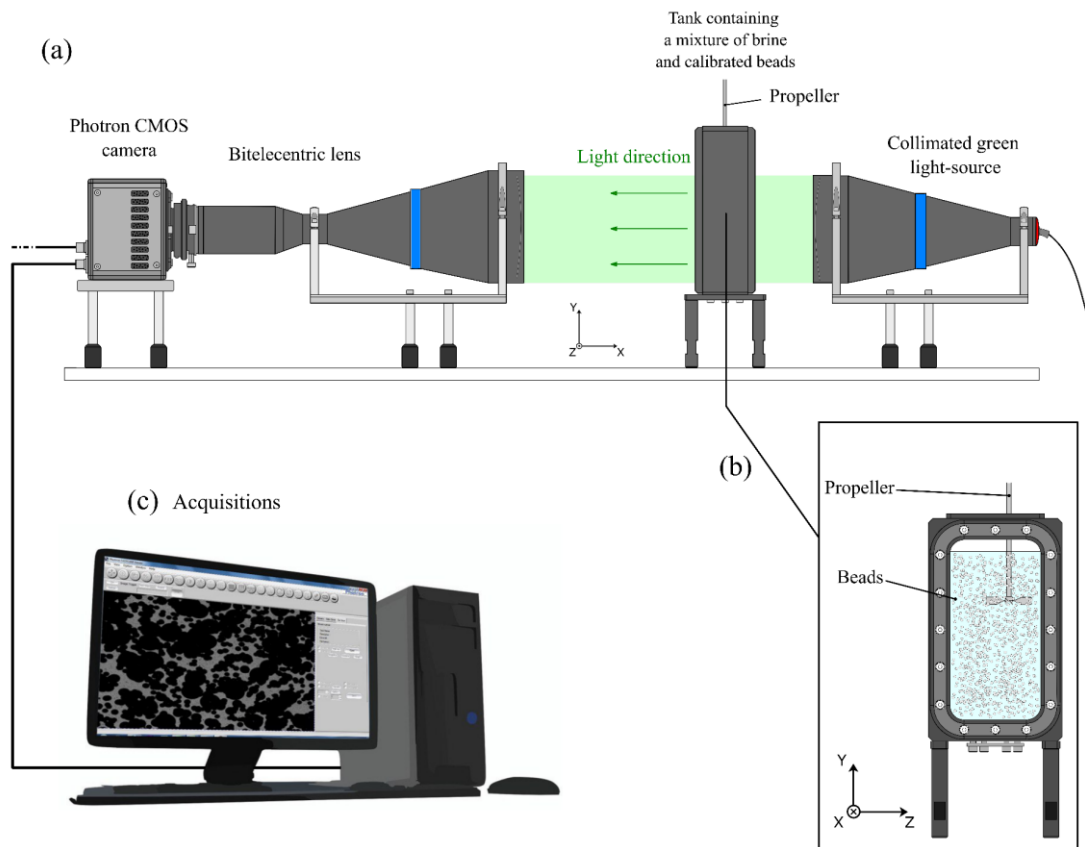
238 Therefore, only four sizes of PMMA particles were used (0.39, 0.5, 0.79 and 1.59 mm in diameter), with four
 239 volume fractions and a fixed PSD. The number of particles used in each experiment was determined by weighing
 240 them with a benchtop precision scale (± 0.2 mg), to evaluate uncertainties on the measured hold-up values. The
 241 various experimental configurations are listed in Table 3.

242 Table 3. Details of the volume fractions and size distributions used for validation experiments with calibrated bead
 243 suspensions.

Experiments	3D hold-up (%)	Size Distribution (PSD)			
	ϕ (\pm scale error)	0.39 mm	0.5 mm	0.79 mm	1.59 mm
1	1.48 ± 0.002	50%	30%	15%	5%
2	2.91 ± 0.003	50%	30%	15%	5%
3	4.31 ± 0.005	50%	30%	15%	5%
4	5.67 ± 0.006	50%	30%	15%	5%

244

245 The mixture was placed in a rectangular tank with external dimensions of $25 \times 15 \times 6.7$ cm³ and a capacity of
 246 1.1 L, fitted with two optical quality windows. The mixture was agitated using a propeller at 2000 rpm to
 247 produce a homogenous flow (Figure 5).



248

249 Figure 5. (a) Side-view sketch of the experiment setup with from left to right, the high speed camera, bi-telecentric lens,
 250 tank, and collimated green light-source. (b) Front view of the tank. (c) Computer with a typical example of a captured image
 251 on the screen ($\phi = 2.91\%$).

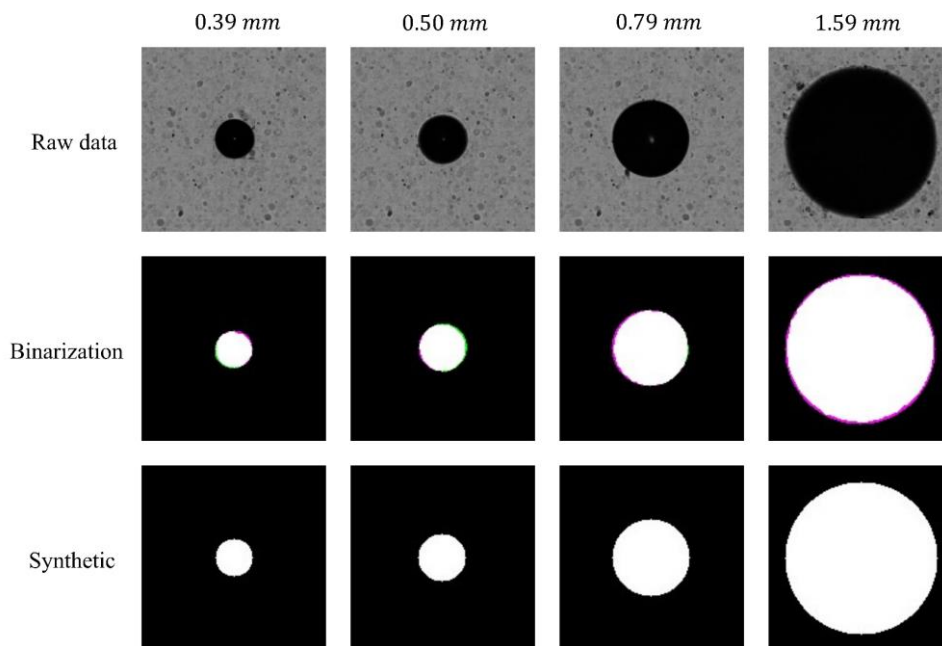
252 Two-dimensional projections of the 3D particle field in the tank were acquired using a backlight setup to avoid
 253 perspective effects. A Photron FASTCAM Mini UX100 CMOS camera was attached to an Opto engineering
 254 TC16M096 bi-telecentric lens placed 26.2 cm from the center of the tank. The tank and sensor were uniformly
 255 illuminated with an Opto engineering collimated green light source (peak wavelength, 525 nm; beam diameter,
 256 120 mm).

257 The captured images consisted of 1280×1024 squared pixels, corresponding to a field of view of $33.7 \times$
 258 29.9 mm^2 (scale factor, $2.6 \times 10^{-2} \text{ mm/px}$). The images were binarized, cropped to 980×980 squared pixels
 259 ($25.8 \times 25.8 \text{ mm}^2$), and resized to 256×256 squared pixels to facilitate coding. The tank was 5.3 cm wide
 260 along the optical axis and covered the entire telecentric field of view, such that the total measurement volume
 261 was 35.3 cm^3 . The images were captured at 50 frames per second, with an exposure time of $1/81\,920 \text{ s}$,
 262 avoiding any motion blur. A set of 4 365 images was acquired for each experiment (Figure 1, first step).

263 The images underwent three steps of preprocessing, starting with a simple binarization using an arbitrary gray
 264 level threshold ($TH = 20$). Morphological area opening using a disk shaped element of 5 pixels was then
 265 applied to denoise the images, removing features such as micro bubbles and dust particles, which appear as small
 266 white dots in the background. The particle contours were then smoothed using an opening operation (erosion
 267 followed by dilatation) with the same structuring element. These morphological operations produce images that
 268 are similar to synthetic images (cf. Figure 6). However, small differences between binarized and simulated
 269 particles can be observed on pixel-by-pixel inspection. The variance between the images can be quantified using
 270 the intersection over union (IoU) ratio between the set of ground truth (synthetic) particles and the set of
 271 binarized particles:

$$272 \quad \text{IoU} = \frac{|A \cap \hat{A}|}{|A \cup \hat{A}|}$$

273 Where A and \hat{A} stand for the simulated and binarized particles respectively, \cap and \cup are respectively the
 274 intersection and union operators, and the vertical bars denote cardinality.



275

276 Figure 6. Comparison between binarized raw data (\hat{A}) and simulated particles (A). Non-intersecting regions are colored in
 277 green for pixels in \hat{A} but not in A and in magenta for pixels in A but not in \hat{A} .

278 The IoU values obtained for all unconnected particles in the dataset (Table 4) show that the discrepancy between
 279 the shapes of the modeled particles and real particles is greater for smaller particles. Moreover, Figure 6 shows

280 that while the model underestimates the size of small particles, larger particles are enlarged in the binarized
281 images. Regardless therefore of the training and the architecture of the machine learning network used,
282 discrepancies between the predictions and the ground truth can be expected, especially for the smallest particles.
283 Note that applying the same morphological operations to the synthetic images did not improve the agreement
284 between the synthetic and binarized images.

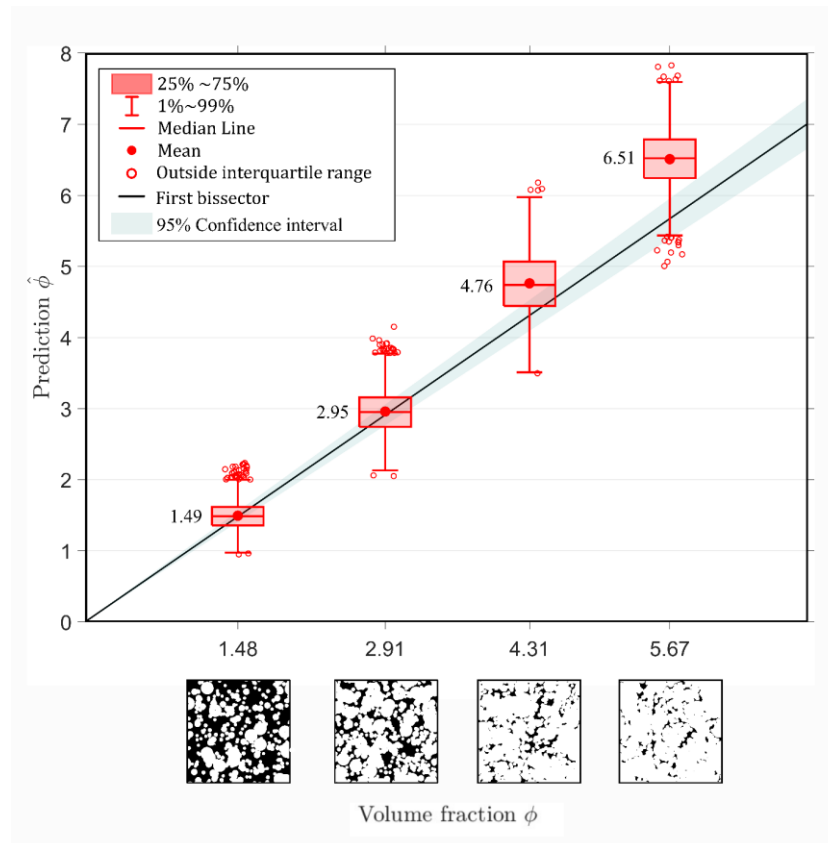
285 Table 4. Intersection over union area for simulated and binarized particles of different sizes.

Particle radius size (<i>mm</i>)	<i>IoU</i>
0.39 mm	0.92
0.50 mm	0.95
0.79 mm	0.97
1.59 mm	0.97

286

287 A new training dataset was generated to retrain CNN^ϕ considering only four particles sizes to mimic the
288 experimental conditions. The distributions of $\hat{\phi}$ values obtained are shown in Figure 7 in separate boxplots for
289 each volume fraction (hold-up).

290



291

292 Figure 7. Boxplot representations of the distribution of predicted hold-up values obtained for each experimental particle
 293 volume fraction. Examples of the experimental images are shown below the corresponding hold-up value. Each boxplot
 294 consists of a red box extending from the first (Q_1) to the third (Q_3) quartile of the distribution and whiskers extending to
 295 $1.5 \times [Q_3 - Q_1]$. Outlier values beyond this range are shown as scattered points. The first bisector (solid line) and 95%
 296 confidence interval (shaded area) are shown to visualize the differences between the average prediction (numerical value on
 297 the left of each box) to the corresponding experimental hold-up ϕ .

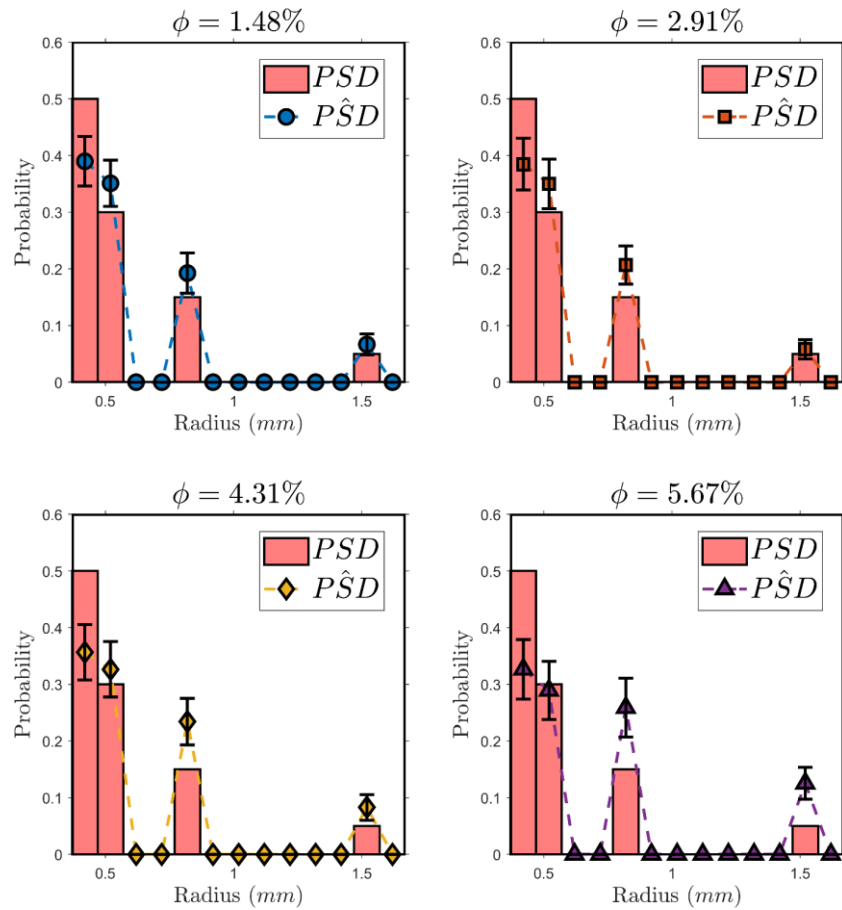
298 These results indicate that the chosen approach was effective for all experimental images. As observed in the
 299 numerical experiments, the predictions tend to become less reliable when the particle density in the image
 300 increases. Whereas more than 25% of the predictions fell within the confidence interval at = 1.48% , this
 301 proportion decreased to 12%, 6% and finally 1% at volume fractions of 2.91%, 4.31% and 5.67%, respectively.
 302 Moreover, Table 5 shows that while the relative error was within the confidence interval ($RE \leq 0.05$) for the
 303 first two experiments, the errors were an order of magnitude larger at higher volume fractions. Figure 8
 304 compares the predicted PSDs with the ground truth for the same four experiments.

305

306 Table 5. Comparison between the average predicted value of the volume fraction ($\hat{\phi}$) and the actual value (ϕ); std, standard
 307 deviation; RE, relative error; MAE, mean absolute error.

Experiments	ϕ (%) (\pm scale error)	Average			
		surface fraction (s/S)	$\hat{\phi}$ (%) (\pm std)	RE	MAE (\pm std)
1	1.48 ± 0.002	45.6%	1.49 ± 0.19	0.008	0.15 ± 0.12
2	2.91 ± 0.003	71.8%	2.95 ± 0.31	0.017	0.25 ± 0.19
3	4.31 ± 0.005	85.4%	4.76 ± 0.44	0.105	0.52 ± 0.37
4	5.67 ± 0.006	92.4%	6.51 ± 0.39	0.148	0.84 ± 0.38

308



309

310 Figure 8. Comparison of predicted particle size distributions (\widehat{PSD}) with the ground truth (PSD) for the four considered
 311 particle volume fractions ϕ .

312 Figure 8 shows that at the two lower volume fractions considered, the CNN correctly recovered the PSD with
 313 only a slight underestimation of the proportion of smallest particles, probably because of the imperfections of the

314 binarization procedure. At higher volume fractions, the PSD was not accurately recovered, the proportion of
 315 larger particles being overestimated, presumably because of particle overlap. The poorer agreement with the
 316 actual PSDs at higher particle volume fractions is reflected by an increase in the corresponding \overline{MAE} s (Table 6).

317 Table 6. \overline{MAE} for the four experimental PSD prediction.

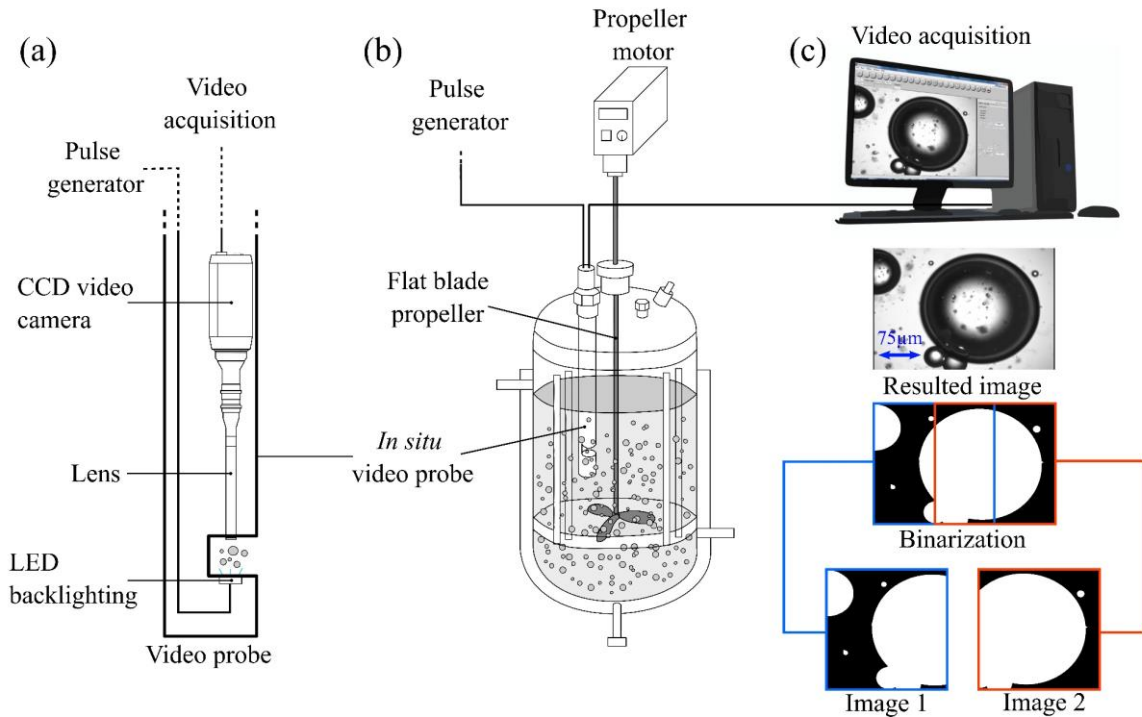
Experiment	\overline{MAE} (\pm std)
1	0.018 \pm 0.006
2	0.019 \pm 0.006
3	0.024 \pm 0.068
4	0.031 \pm 0.008

318

319 4.2. Validation for a liquid-liquid system

320 The approach was further validated using previously acquired data (Amokrane et al., 2014). Images of water
 321 droplets in a emulsion with tetra-propylene hydrogen (TPH, density $\rho = 760 \text{ kg/m}^3$; viscosity $\eta = 1.26 \times$
 322 $10^{-3} \text{ Pa} \cdot \text{s}$; surface tension $\gamma = 43 \times 10^{-3} \text{ N/m}$) were obtained using an in-situ video camera placed inside a
 323 cylindrical stirred tank reactor (internal volume, 1 L; internal height, H ; Figure 9 (b)). Emulsions with hold-ups
 324 of up to 5% were stirred at 500 rpm with a three-flat-blade propeller (diameter, 60 mm) placed $H/3$ above the
 325 base of the vessel. Images were acquired after 60 min of stirring to ensure that a steady state had been reached.

326 The probe consisted of a CCD camera with LED back lighting (Figure 9 (a)). Images were obtained of the
 327 emulsion flowing through a 1500 μm wide gap between the LED and the lens. The images were $710 \times 480 \text{ px}^2$
 328 in size with a resolution of 2 $\mu\text{m}/\text{px}$ allowing the detection of droplets larger than 8 μm in diameter. The images
 329 were then split into two $480 \times 480 \text{ px}^2$ square images (Figure 9 (c)); to double the number of acquired images.
 330 Further information on the experimental setup and the fluids can be found in Khalil et al. (Khalil et al., 2010).



331

332 Figure 9. Schematic diagrams of the setup used to obtain images of a water-in-TPH emulsion. (a) Diagram of the video probe

333 used to capture the images of the emulsion flowing through the gap between the lens and the LED. (b) Diagram of the

334 double-jacketed cylindrical tank containing the emulsion, the video probe and the propeller used to stir the mixture. (c)

335 Examples of the raw images obtained, after binarization, and after cropping.

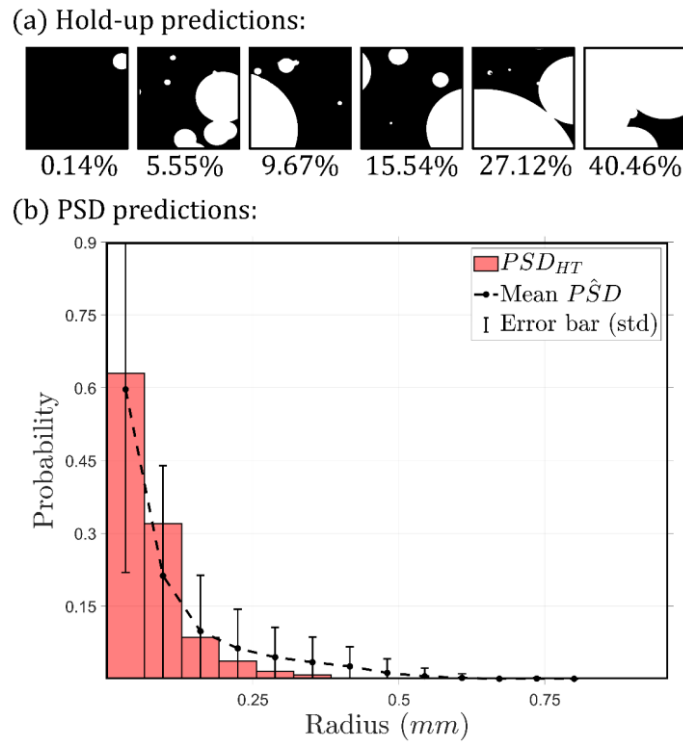
336 The volume fraction and the PSD were retrieved from 3 870 images. In this experiment, the volume fraction

337 could be controlled but the PSD of the dispersed phase was unknown. The predicted PSDs were therefore

338 compared with values obtained by the Hough transform (Amokrane et al., 2014). The two machine learning

339 networks, CNN^ϕ and CNN^{PSD} , were retrained on a new simulated dataset corresponding to the experimental340 setup, consisting of 240×240 pixel images in three channels ($240 \times 240 \times 3 \text{ px}^3$) as before.

341



342

343

344

345

Hough transform PSDs (\widehat{PSD} vs PSD_{HT}).

346

347

348

349

350

351

352

353

354 5. Conclusion and perspectives

355

356

357

358

This article describes a new image processing technique for dense flow imaging, combining a stochastic geometrical model with convolutional neural networks to retrieve 3D properties of particle systems using only 2D projected images. Using this approach, the volume fraction of the dispersed phase and the particle size distribution are predicted directly from the images. A stochastic model was developed to generate training

359 images labeled with the targeted 3D properties of the system. Two CNN architectures were built, one to quantify
 360 the volume fraction of the observed particle field and the other to recover the PSD. After numerical validation on
 361 simulated images, the approach was validated on experimental images of calibrated beads and of an emulsion in
 362 a tank. Results confirm that average 3D quantities can be measured using this approach from a single optical
 363 access, even for flows with high-dispersed phase volume fractions. In particular, this new approach remains
 364 effective in the presence of high particle overlap, where traditional image-processing techniques typically fail.
 365 The approach is also computationally efficient, with the analysis of thousands of images typically completed in
 366 less than 30 min. Moreover, the method is easy to implement and can readily be re-purposed by transfer learning
 367 to study different types of multiphase flows, making it suitable for many applications in chemical engineering.
 368 These encouraging results highlight the value of combining a stochastic geometry model with deep learning to
 369 predict 3D information. Note that while a lognormal function was used for the PSD in this study, the model can
 370 be trained to predict any type of discrete distribution. The model could also be extended to study ellipsoidal
 371 particles, which are more representative of gas-liquid flow. This should be relatively straightforward since
 372 Matern type II models for ellipsoidal shapes have already been described in the literature (de Langlard et al.,
 373 2018b).

374 Future work will focus in the short term on improving the stochastic model by including spatial heterogeneity
 375 and more complex shapes (e.g. cap-shaped or skirted particles); to better account for spatial inhomogeneities in
 376 the flow images and the variety of particle shapes typically encountered in dispersed phases of multiphase flows.
 377 Also, more complex CNN architectures will be studied in order to improve the results and treat irregular shapes
 378 (Ma et al., 2022; Murata et al., 2020).

379 **List of symbols and abbreviations**

Symbols

W	Observation window (m^2)
l	Length of the projection direction (m)
r_i	Radius of the i th particle
t_i	Time of birth of the i th particle
n_p	Total number of particles
n	Number of outputs for CNN^{PSD}

N_t	Number of training images
N_v	Number of validation images
N_e	Number of testing images
N	Total number of generated images ($N = N_t + N_v + N_e$)
\mathcal{L}_{tr}	Truncated Lognormal law
a	First support of the truncated law
b	Second support of the truncated law
n_j	Number of particles in the j th class
d_j	Diameter of the j th class (m)
v_i	Total volume of the dispersed phase in the i th image (m ³)
V_i	Total volume of the mixture in the i th image (m ³)
ϕ_i	Volume fraction of the i th image
$\hat{\phi}_i$	Predicted volume fraction of the i th image
PSD_i	Particle size distribution of the i th image
$P\hat{S}D_i$	Predicted particle size distribution of the i th image
s^2	Variance
\bar{d}	Mean diameter (m)
A	Synthetic particle image
\check{A}	Binarized particle image
s/S	Surface fraction
$\overline{\text{MAE}}$	Overall Mean Absolute Error

Greek Symbols

γ	Surface tension (N/m)
η	Viscosity (Pa.s)
λ	Point process intensity
μ, σ	Lognormal parameters
ρ	Density (kg/m ³)
ϕ	Hold-up or Volume fraction of the dispersed phase

Abbreviations

3D	Three-dimensional
2D	Two-dimensional
CNN	Convolutional Neural Network
CNN ^ϕ	Network for predicting volume fraction
CNN ^{PSD}	Network for predicting particle size distribution
DL	Deep Learning
DIH	Digital In-line Holography
FC layer	Fully Connected layer
FIB-SEM	Focused Ion Beam-Scanning Electron Microscope
FBRM	Focused Beam Reflectance Measurement
MAE	Mean Absolute Error
OMAE	Global Mean Absolute Error
PMMA	Poly (Methyl Methacrylate)
PSD	Particle Size Distribution
RE	Relative Error
std	Standard Deviation
IoU	Intersection over Union

380 **References**

- 381 Acevedo, D., Wu, W.L., Yang, X., Pavurala, N., Mohammad, A., O'Connor, T.F., 2021. Evaluation of focused
382 beam reflectance measurement (FBRM) for monitoring and predicting the crystal size of carbamazepine in
383 crystallization processes. *CrystEngComm* 23, 972–985. <https://doi.org/10.1039/d0ce01388a>
- 384 Amokrane, A., Charton, S., Sheibat-Othman, N., Becker, J., Klein, J.P., Puel, F., 2014. Development of a CFD-
385 PBE coupled model for the simulation of the drops behaviour in a pulsed column. *Can. J. Chem. Eng.* 92,
386 220–233. <https://doi.org/10.1002/cjce.21933>
- 387 Black, D.L., McQuay, M.Q., Bonin, M.P., 1996. Laser-based techniques for particle-size measurement: A
388 review of sizing methods and their industrial applications. *Prog. Energy Combust. Sci.* 22, 267–306.
389 [https://doi.org/10.1016/S0360-1285\(96\)00008-1](https://doi.org/10.1016/S0360-1285(96)00008-1)

- 390 Boxall, J.A., Koh, C.A., Sloan, E.D., Sum, A.K., Wu, D.T., 2010. Measurement and Calibration of Droplet Size
391 Distributions in Water-in-Oil Emulsions by Particle Video Microscope and a Focused Beam Reflectance
392 Method. *Ind. Eng. Chem. Res.* 49, 1412–1418. <https://doi.org/10.1021/ie901228e>
- 393 Chen, Q., Yang, X., Petriu, E.M., 2004. Watershed segmentation for binary images with different distance
394 transforms. *Proc. - 3rd IEEE Int. Work. Haptic, Audio Vis. Environ. their Appl. - HAVE 2004* 111–116.
395 <https://doi.org/10.1109/have.2004.1391891>
- 396 Clift, R., Grace, J. R., & Weber, M.E., 2005. Bubbles, drops, and particles.
- 397 Couto, H.J.B., Nunes, D.G., Neumann, R., França, S.C.A., 2009. Micro-bubble size distribution measurements
398 by laser diffraction technique. *Miner. Eng.* 22, 330–335. <https://doi.org/10.1016/j.mineng.2008.09.006>
- 399 Cui, Y., Li, C., Zhang, W., Ning, X., Shi, X., Gao, J., Lan, X., 2022. A deep learning-based image processing
400 method for bubble detection, segmentation, and shape reconstruction in high gas holdup sub-millimeter
401 bubbly flows. *Chem. Eng. J.* 449, 137859. <https://doi.org/10.1016/j.cej.2022.137859>
- 402 Darakis, E., Khanam, T., Rajendran, A., Kariwala, V., Naughton, T.J., Asundi, A.K., 2010. Microparticle
403 characterization using digital holography. *Chem. Eng. Sci.* 65, 1037–1044.
404 <https://doi.org/10.1016/j.ces.2009.09.057>
- 405 de Langlard, M., Al-Saddik, H., Charton, S., Debayle, J., Lamadie, F., 2018a. An efficiency improved
406 recognition algorithm for highly overlapping ellipses: Application to dense bubbly flows. *Pattern Recognit.*
407 *Lett.* 101, 88–95. <https://doi.org/10.1016/j.patrec.2017.11.024>
- 408 de Langlard, M., Lamadie, F., Charton, S., Debayle, J., 2018b. A 3D stochastic model for geometrical
409 characterization of particles in two-phase flow applications. *Image Anal. Stereol.* 37, 233–247.
410 <https://doi.org/10.5566/ias.1942>
- 411 Dia, K., Lamadie, F., Debayle, J., 2022. Using deep learning to retrieve 3D geometrical characteristics of a
412 particle field from 2D projected images: Application to multiphase flows, in: *2022 12th International*
413 *Conference on Pattern Recognition Systems (ICPRS)*. IEEE, pp. 1–7.
414 <https://doi.org/10.1109/ICPRS54038.2022.9854059>
- 415 Emmerich, J., Tang, Q., Wang, Y., Neubauer, P., Junne, S., Maaß, S., 2019. Optical inline analysis and
416 monitoring of particle size and shape distributions for multiple applications: Scientific and industrial

- 417 relevance. *Chinese J. Chem. Eng.* 27, 257–277. <https://doi.org/10.1016/j.cjche.2018.11.011>
- 418 Fend, C., Moghiseh, A., Redenbach, C., Schladitz, K., 2021. Reconstruction of highly porous structures from
419 FIB-SEM using a deep neural network trained on synthetic images. *J. Microsc.* 281, 16–27.
420 <https://doi.org/10.1111/jmi.12944>
- 421 Gianinoni, I., Golinelli, E., Melzi, G., Musazzi, S., Perini, U., Trespidi, F., 2003. Optical particle sizers for on-
422 line applications in industrial plants. *Opt. Lasers Eng.* 39, 141–154. [https://doi.org/10.1016/S0143-](https://doi.org/10.1016/S0143-8166(01)00090-2)
423 [8166\(01\)00090-2](https://doi.org/10.1016/S0143-8166(01)00090-2)
- 424 Haas, T., Schubert, C., Eickhoff, M., Pfeifer, H., 2020. BubCNN: Bubble detection using Faster RCNN and
425 shape regression network. *Chem. Eng. Sci.* 216, 115467. <https://doi.org/10.1016/j.ces.2019.115467>
- 426 Heath, A.R., Fawell, P.D., Bahri, P.A., Swift, J.D., 2002. Estimating Average Particle Size by Focused Beam
427 Reflectance Measurement (FBRM). *Part. Part. Syst. Character.* 19, 84. [https://doi.org/10.1002/1521-](https://doi.org/10.1002/1521-4117(200205)19:2<84::AID-PPSC84>3.0.CO;2-1)
428 [4117\(200205\)19:2<84::AID-PPSC84>3.0.CO;2-1](https://doi.org/10.1002/1521-4117(200205)19:2<84::AID-PPSC84>3.0.CO;2-1)
- 429 Heinrich, J., Ulrich, J., 2012. Application of Laser-Backscattering Instruments for In Situ Monitoring of
430 Crystallization Processes - A Review. *Chem. Eng. Technol.* 35, 967–979.
431 <https://doi.org/10.1002/ceat.201100344>
- 432 Honkanen, M., Eloranta, H., Saarenrinne, P., 2010. Digital imaging measurement of dense multiphase flows in
433 industrial processes. *Flow Meas. Instrum.* 21, 25–32. <https://doi.org/10.1016/j.flowmeasinst.2009.11.001>
- 434 Huang, X., Kakuda, Y., Cui, W., 2001. Hydrocolloids in emulsions: Particle size distribution and interfacial
435 activity. *Food Hydrocoll.* 15, 533–542. [https://doi.org/10.1016/S0268-005X\(01\)00091-1](https://doi.org/10.1016/S0268-005X(01)00091-1)
- 436 Iqbal, H., 2018. PlotNeuralNet. <https://doi.org/10.5281/zenodo.2526396>
- 437 Juliá, J.E., Hartevelde, W.K., Mudde, R.F., Van Den Akker, H.E.A., 2005. On the accuracy of the void fraction
438 measurements using optical probes in bubbly flows. *Rev. Sci. Instrum.* 76.
439 <https://doi.org/10.1063/1.1862192>
- 440 Karn, A., Ellis, C., Arndt, R., Hong, J., 2015. An integrative image measurement technique for dense bubbly
441 flows with a wide size distribution. *Chem. Eng. Sci.* 122, 240–249.
442 <https://doi.org/10.1016/j.ces.2014.09.036>
- 443 Kavanaugh, M.C., Tate, C.H., Trussell, A.R., Trussell, R.R., Treweek, G., 1980. Use of particle size distribution

- 444 measurements for selection and control of solid/liquid separation processes. Part. Water Charact. Fate, Eff.
445 Removal, M.C. Kavanaugh; J.O. Leckie (Eds.), Washington, D.C., 305–328. <https://doi.org/10.1021/ba->
446 1980-0189.ch014
- 447 Khalil, A., Puel, F., Chevalier, Y., Galvan, J.M., Rivoire, A., Klein, J.P., 2010. Study of droplet size distribution
448 during an emulsification process using in situ video probe coupled with an automatic image analysis.
449 Chem. Eng. J. 165, 946–957. <https://doi.org/10.1016/j.cej.2010.10.031>
- 450 Kim, Y., Park, H., 2021. Deep learning-based automated and universal bubble detection and mask extraction in
451 complex two-phase flows. Sci. Rep. 11, 8940. <https://doi.org/10.1038/s41598-021-88334-0>
- 452 Lamadie, F., Bruel, L., Himbert, M., 2012. Digital holographic measurement of liquid-liquid two-phase flows.
453 Opt. Lasers Eng. 50, 1716–1725. <https://doi.org/10.1016/j.optlaseng.2012.07.010>
- 454 Lau, Y.M., Deen, N.G., Kuipers, J.A.M., 2013. Development of an image measurement technique for size
455 distribution in dense bubbly flows. Chem. Eng. Sci. 94, 20–29. <https://doi.org/10.1016/j.ces.2013.02.043>
- 456 Li, J., Shao, S., Hong, J., 2021. Machine learning shadowgraph for particle size and shape characterization.
457 Meas. Sci. Technol. 32. <https://doi.org/10.1088/1361-6501/abae90>
- 458 Ma, L., Kashanj, S., Xu, S., Zhou, J., Nobes, D.S., Ye, M., 2022. Flow Reconstruction and Prediction Based on
459 Small Particle Image Velocimetry Experimental Datasets with Convolutional Neural Networks. Ind. Eng.
460 Chem. Res. 61, 8504–8519. <https://doi.org/10.1021/acs.iecr.1c04704>
- 461 Maaß, S., Wollny, S., Voigt, A., Kraume, M., 2011. Experimental comparison of measurement techniques for
462 drop size distributions in liquid/liquid dispersions. Exp. Fluids 50, 259–269.
463 <https://doi.org/10.1007/s00348-010-0918-9>
- 464 Matérn, B., 2014. Spatial Variation, Encyclopedia of Environmental Change.
465 <https://doi.org/10.4135/9781446247501.n3658>
- 466 Murata, T., Fukami, K., Fukagata, K., 2020. Nonlinear mode decomposition with convolutional neural networks
467 for fluid dynamics. J. Fluid Mech. 882, 1–15. <https://doi.org/10.1017/jfm.2019.822>
- 468 Panckow, R.P., Reinecke, L., Cuellar, M.C., Maaß, S., 2017. Photo-Optical In-Situ Measurement of Drop Size
469 Distributions: Applications in Research and Industry. Oil Gas Sci. Technol. – Rev. d'IFP Energies Nouv.
470 72, 14. <https://doi.org/10.2516/ogst/2017009>

- 471 Pandalaneni, K., Amamcharla, J.K., 2016. Focused beam reflectance measurement as a tool for in situ
472 monitoring of the lactose crystallization process. *J. Dairy Sci.* 99, 5244–5253.
473 <https://doi.org/10.3168/jds.2015-10643>
- 474 Pandit, A., Katkar, V., Ranade, V., Bhambure, R., 2019. Real-Time Monitoring of Biopharmaceutical
475 Crystallization: Chord Length Distribution to Crystal Size Distribution for Lysozyme, rHu Insulin, and
476 Vitamin B12. *Ind. Eng. Chem. Res.* 58, 7607–7619. <https://doi.org/10.1021/acs.iecr.8b04613>
- 477 Poelma, C., 2020. Measurement in opaque flows: a review of measurement techniques for dispersed multiphase
478 flows. *Acta Mech.* 231, 2089–2111. <https://doi.org/10.1007/s00707-020-02683-x>
- 479 Ruf, A., Worlitschek, J., Mazzotti, M., 2000. Modeling and Experimental Analysis of PSD Measurements
480 through FBRM. *Part. Part. Syst. Charact.* 17, 167–179. [https://doi.org/10.1002/1521-4117\(200012\)17:4<167::AID-PPSC167>3.0.CO;2-T](https://doi.org/10.1002/1521-4117(200012)17:4<167::AID-PPSC167>3.0.CO;2-T)
- 482 Sentis, M.P.L., Bruel, L., Charton, S., Onofri, F.R.A., Lamadie, F., 2017. Digital in-line holography for the
483 characterization of flowing particles in astigmatic optical systems. *Opt. Lasers Eng.* 88, 184–196.
484 <https://doi.org/10.1016/j.optlaseng.2016.08.012>
- 485 Shao, S., Mallery, K., Hong, J., 2020. Machine learning holography for measuring 3D particle distribution.
486 *Chem. Eng. Sci.* 225. <https://doi.org/10.1016/j.ces.2020.115830>
- 487 Sheng, J., Malkiel, E., Katz, J., 2006. Digital holographic microscope for measuring three-dimensional particle
488 distributions and motions. *Appl. Opt.* 45, 3893–3901. <https://doi.org/10.1364/AO.45.003893>
- 489 Stoyan, D., Stoyan, H., 1985. On One of Matérn's Hard-core Point Process Models. *Math. Nachrichten* 122,
490 205–214. <https://doi.org/10.1002/mana.19851220121>
- 491 Suh, Y., Bostanabad, R., Won, Y., 2021. Deep learning predicts boiling heat transfer. *Sci. Rep.* 11, 1–10.
492 <https://doi.org/10.1038/s41598-021-85150-4>
- 493 Wang, H.Y., Shi, Y.F., Zhu, X.J., Song, L.M., Dong, F., 2022. 3-D Reconstruction of Bubble Flow Field Based
494 on the Method of Multivision by Rough-Precise Location Algebraic Reconstruction Technique. *IEEE*
495 *Trans. Instrum. Meas.* 71. <https://doi.org/10.1109/TIM.2022.3158993>
- 496 Xue, T., Qu, L., Wu, B., 2014. Matching and 3-D reconstruction of multibubbles based on virtual stereo vision.
497 *IEEE Trans. Instrum. Meas.* 63, 1639–1647. <https://doi.org/10.1109/TIM.2013.2289586>

- 498 Yang, Y., Kang, B.S., 2011. Digital particle holographic system for measurements of spray field characteristics.
499 Opt. Lasers Eng. 49, 1254–1263. <https://doi.org/10.1016/j.optlaseng.2011.06.017>
- 500 Yu, X., Xing, D., Hazuku, T., Takamasa, T., Ishimaru, T., Tanaka, Y., Akiba, T., 2009. Measurement technique
501 for solid-liquid two-phase flow using a Normal-line Hough Transform method. J. Phys. Conf. Ser. 147,
502 012053. <https://doi.org/10.1088/1742-6596/147/1/012053>
- 503 Zafari, S., Murashkina, M., Eerola, T., Sampo, J., Kälviäinen, H., Haario, H., 2020. Resolving overlapping
504 convex objects in silhouette images by concavity analysis and Gaussian process. J. Vis. Commun. Image
505 Represent. 73, 102962. <https://doi.org/10.1016/j.jvcir.2020.102962>
- 506 Zhang, W.H., Jiang, X., Liu, Y.M., 2012. A method for recognizing overlapping elliptical bubbles in bubble
507 image. Pattern Recognit. Lett. 33, 1543–1548. <https://doi.org/10.1016/j.patrec.2012.03.027>
- 508 Zou, T., Pan, T., Taylor, M., Stern, H., 2021. Recognition of overlapping elliptical objects in a binary image.
509 Pattern Anal. Appl. 24, 1193–1206. <https://doi.org/10.1007/s10044-020-00951-z>
- 510